BATTERIES

Decoupling the air sensitivity of Na-layered oxides

Yang Yang[1,2]†, Zaifa Wang[3]†, Congcong Du[3], Bowen Wang[1,2], Xinyan Li[1,2], Siyuan Wu[1,2], Xiaowei Li[4], Xiao Zhang[1,2], Xubin Wang[1,2], Yaoshen Niu[1], Feixiang Ding[1], Xiaohui Rong[5]*, Yaxiang Lu[1,6]*, Nian Zhang[7], Juping Xu[8], Ruijuan Xiao[1], Qinghua Zhang[1], Xuefeng Wang[1], Wen Yin[8], Junmei Zhao[4], Liquan Chen[1], Jianyu Huang[3]*, Yong-Sheng Hu[1,2,6]*

Air sensitivity remains a substantial barrier to the commercialization of sodium (Na)–layered oxides (NLOs). This problem has puzzled the community for decades because of the complexity of interactions between air components and their impact on both bulk and surfaces of NLOs. We show here that water vapor plays a pivotal role in initiating destructive acid and oxidative degradations of NLOs only when coupled with carbon dioxide or oxygen, respectively. Quantification analysis revealed that reducing the defined cation competition coefficient (η), which integrates the effects of ionic potential and sodium content, and increasing the particle size can enhance the resistance to acid attack, whereas using high-potential redox couples can eliminate oxidative degradation. These findings elucidate the underlying air deterioration mechanisms and rationalize the design of air-stable NLOs.

Layered metal oxides hold promise as cathode materials for both Li-ion batteries (LIBs) and Na-ion batteries (NIBs) because of their exceptional capacity and scalability (*1*–*5*). Compared with Li-layered oxides, (LLOs), Na-layered oxides (NLOs, with the formula Na_xTMO_2, where TM represents transition metals) suffer from a critical challenge: Even in the absence of Ni-rich design, which is the primary cause of instability in LLOs (*6*–*8*), they still rapidly degrade within hours because of extreme sensitivity to air exposure. This issue can result in capacity loss, electrode manufacturing difficulties, and inferior performance (fig. S1) (*9*). This air instability has been hindering the comprehensive utilization of NLOs for >40 years (*10*–*12*), so resolving this problem becomes paramount for unlocking their potential to revolutionize the energy storage landscape and accelerate the development of practical NIBs (*13*–*16*).

Understanding the origin of instability begins with understanding the interactions between the air and NLOs. However, the coupled atmospheric composition, precovered residues, and environmental effects in postmortem characterizations can veil the clear degradation pathways. This has led to various degradation models, including the water molecular intercalation (*11*, *12*), the oxidation of TM by O_2 or H_2O (*9*), the direct reaction between CO_2 and residues at the surface or in the bulk (*17*, *18*), the uptake of CO_2 and H_2O with the intercalation of carbonate ion (*19*), and the exchange of Na^+/H^+ or Na^+/H_3O^+ with water (*20*–*22*). Although controversial, the devastating role of water vapor on its own is widely emphasized, and will be challenged by our findings here. In addition to the unclear mechanism, the lack of a standard method and quantitative analysis further impedes the precise evaluation of the air stability of different NLOs, thereby obscuring the design principles. Therefore, a comprehensive understanding of the air instability issue and a rational design of air-stable NLOs are urgently demanded.

We chose O3-$NaNi_{1/3}Fe_{1/3}Mn_{1/3}O_2$ (NFM111) as our model system. It is a material that has been extensively studied for its high capacity and scalability but is restricted by poor air stability (*23*–*26*). Through a combination of ex situ and in situ observations, we observed that water vapor does not inherently destroy NFM111 and its analog, but acts as a pivotal factor leading to distinct acid and oxidative degradation collectively with CO_2 and O_2, respectively.

Decoupling the roles of different air components

The as-synthesized NFM111 exhibits a pure O3 phase ($R\bar{3}M$) and a clean surface, as confirmed by x-ray diffraction (XRD), scanning electron microscopy (SEM), and transmission electron microscopy (TEM) (fig. S2 and table S1). In situ XRD patterns (Fig. 1A) showed that NFM111 degrades within hours upon exposure to the air at a relative humidity (RH) of 50%. The (003) peak shifts to a lower angle, whereas the (110) peak shifts to a higher angle immediately after air exposure, reflecting an enlargement a[illegible] the *c*-axis and a shrinkage along the *a*-axi[illegible] Na^+ is deintercalated. New peaks of Na_2CO_3 appear within 3 hours of air exposure. The water-intercalated phase (main peak at 12.5°), which is frequently observed in P2-Na_xTMO_2 ($x < 0.7$), is not visible in degraded NFM111. This may be attributed to the relatively higher Na content and narrower Na layer in O3-Na_xTMO_2 ($0.8< x \leq 1$), which retard the hydration process at low Na content (*22*). However, >50% of the pristine specific capacity of NFM111 is irreversibly lost after air exposure for 48 hours (Fig. 1B), whereas it might be recovered in degraded P2-Na_xTMO_2 upon discharge, with the Na metal anode providing extra Na^+ (*21*, *27*). This emphasizes the more severe effects that air instability has on O3-Na_xTMO_2. Further, the true capacity of NFM111, and even the O3-Na_xTMO_2 family, is underestimated solely because of the poor air stability, as indicated by the much higher capacity of the as-synthesized NFM111 (146 mAh g^{-1}) compared with the conventionally processed sample (~120 mAh g^{-1}) in previous comparable reports (*24*, *25*).

To initially determine which gases govern the degradation, NFM111 samples were first stored in six combinations of three key air components for 48 hours and then characterized by XRD and SEM. The strictly controlled atmospheres include water vapor (N_2 protected, RH = 90%), pure O_2 (RH = 0%), pure CO_2 (RH = 2%, trace water can be detected even being stored with P_2O_5), O_2 with water vapor (RH = 80%), O_2 with CO_2 (RH = 2%), and CO_2 with water vapor (RH = 70%). For simplicity, the obtained samples are denoted as H-48, O-48, C-48, HO-48, CO-48, and HC-48, respectively (detailed conditions and nomenclature are summarized in fig. S3 and table S2). Conventional intuition suggests that any one of the three gases, but in particular water vapor or CO_2, can lead to severe deterioration. The XRD pattern (Fig. 1C) of H-48 does not show any new peaks or an obvious shift of peaks under such high RH. Even after prolonged exposure to water vapor for 1 week (H-1W), NFM111 still retains its original peak positions. The same trends were observed for O-48 and C-48, with a slightly reduced crystallinity in C-48. These results suggest that the three key gases are not individually catastrophic to the global structure of NFM111. Rather, the synergic effects from the combined gases are more vital. The unchanged XRD pattern of CO-48 suggests that the degradation requires the presence of water vapor. When both water vapor and O_2 are present, moderate peak shifts are found in the XRD pattern of HO-48. The combination of water vapor and CO_2 causes significant peak shifts, along with the vanishing of O3 phase peaks and the appearance of $NaHCO_3$ peaks in the XRD pattern of HC-48 (a magnified comparison of XRD patterns is included in fig. S4).

[1]Key Laboratory for Renewable Energy, Beijing Key Laboratory for New Energy Materials and Devices, Beijing National Laboratory for Condensed Matter Physics, Institute of Physics, Chinese Academy of Sciences, Beijing 100190, China. [2]College of Materials Science and Optoelectronic Technology, University of Chinese Academy of Sciences, Beijing 100049, China. [3]Clean Nano Energy Center, State Key Laboratory of Metastable Materials Science and Technology, Yanshan University, Qinhuangdao 066000, China. [4]Institute of Process Engineering, Chinese Academy of Sciences, Beijing 100190, China. [5]Yangtze River Delta Physics Research Center Co. Ltd., Liyang 213300, China. [6]Huairou Division, Institute of Physics, Chinese Academy of Sciences, Beijing 101400, China. [7]State Key Laboratory of Functional Materials for Informatics, Shanghai Institute of Microsystem and Information Technology (SIMIT), Chinese Academy of Sciences, Shanghai 200050, China. [8]Spallation Neutron Source Science Center (SNSSC), Dongguan 523803, China.
***Corresponding author. Email: rongxiaohui@ioply.cn (X.R.); yxlu@iphy.ac.cn (Y.L.); jyhuang8@hotmail.com (J.H.); yshu@iphy.ac.cn (Y.-S.H.)**
†These authors contributed equally to this work.

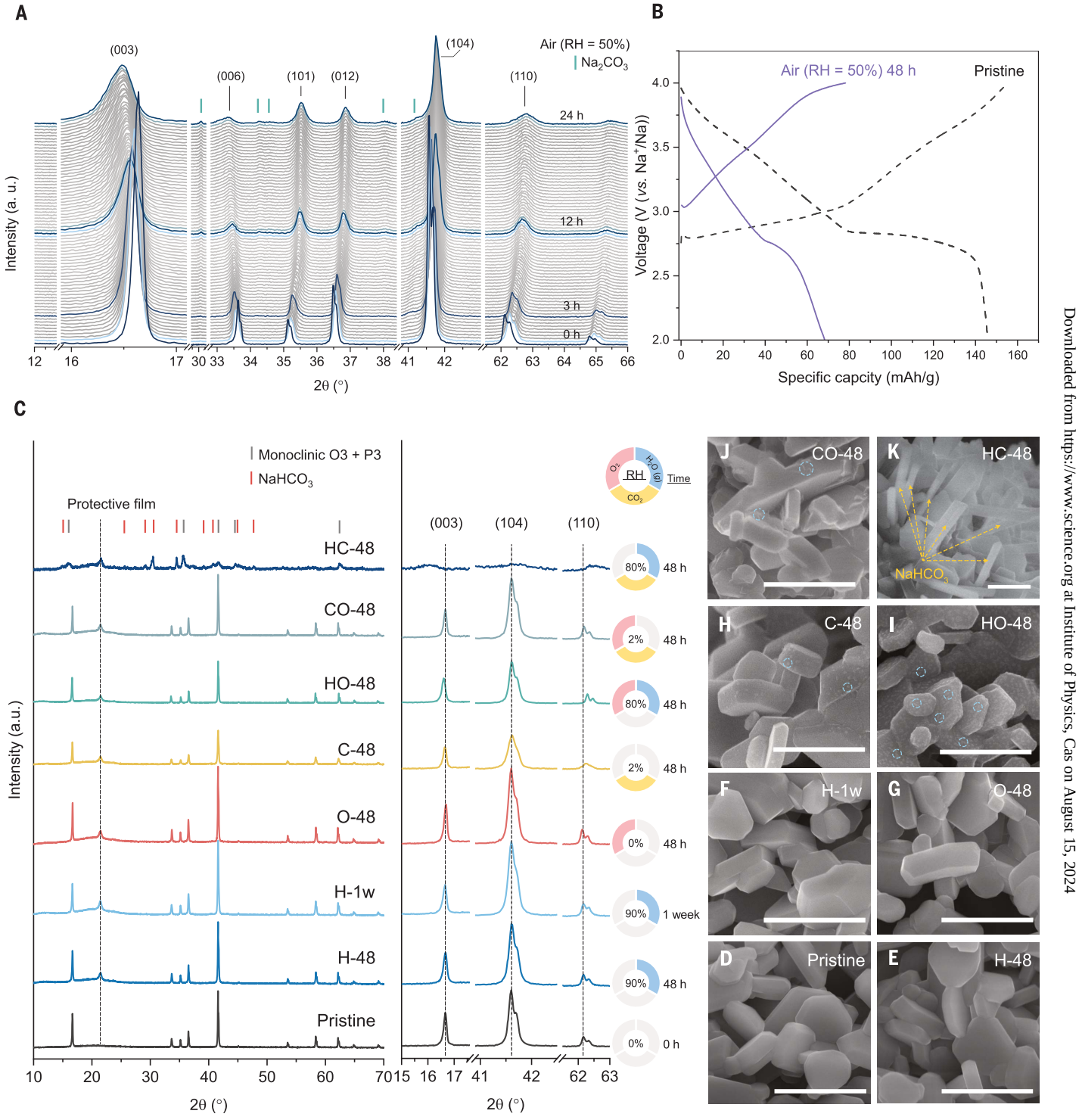

Fig. 1. Structural, morphological evolutions, and capacity loss of NFM111 upon exposure to different atmospheres. (**A**) In situ XRD patterns of NFM111 exposed to air (RH = 50%) for 24 hours. (**B**) Galvanostatic charge/discharge voltage profiles of fresh and air exposed NFM111 (RH = 50% for 48 hours) in the initial cycle in the voltage range of 2.0 to 4.0 V (versus Na^+/Na) at a rate of 0.2C (30 mA g^{-1}). (**C**) XRD patterns of NFM111 exposed to different atmospheres with magnified regions of (003), (104), and (110). The corresponding atmospheres are represented by various combinations of three fundamental gases in the ring-like legends (right), where the three split gray parts are colored blue, yellow, and red, respectively, when water vapor, CO_2, and O_2 are present. The RH and processing time are also indicated on the inside and outside of the ring, respectively. (**D** to **K**) SEM images of NFM111 after being exposed to different atmospheres. Protuberances are marked with circles in (H) to (J). Scale bars, 1 μm in (D) to (K).

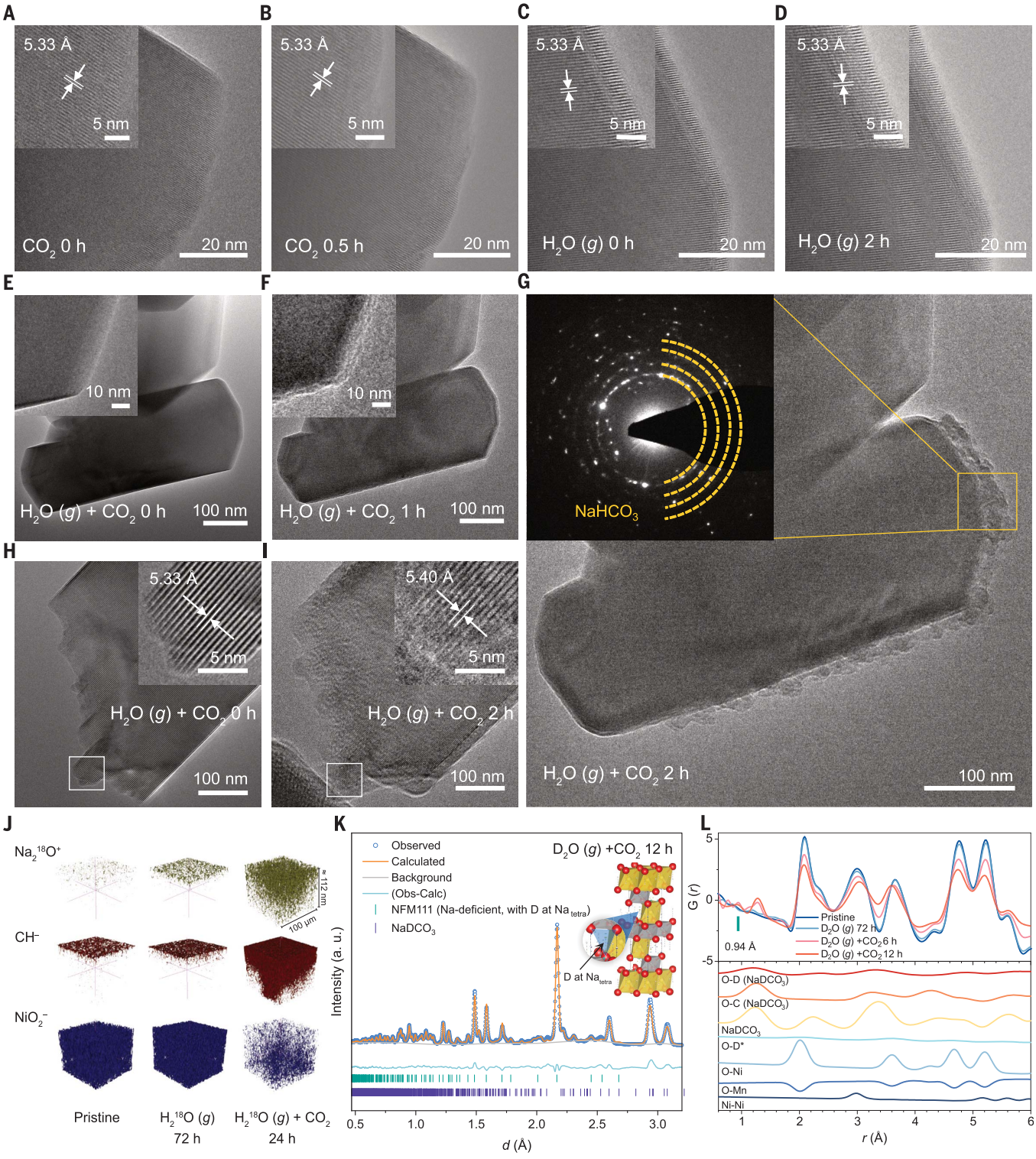

Fig. 2. Acid degradation characterized by dynamic observation and isotope-labeling strategies. (**A** to **I**) In situ ETEM images of clean nanocrystals of NFM111 before (A) and after (B) CO_2 exposure for 30 min (p = 7 mbar); before (C) and after (D) water vapor exposure for 2 hours (p = 0.5 mbar); before [(E) and (H)] and after water vapor and CO_2 exposure for 1 hour (F) and 2 hours [(G) and (I)] (p_{total} = 0.5 mbar). (**J**) 3D rendering of selected representative secondary-ion fragments from ToF-SIMS characterization. Samples were stored in N_2 with $H_2{}^{18}O$ vapor for 72 hours and in CO_2 with $H_2{}^{18}O$ vapor for 24 hours. (**K**) Refinement of the NPD pattern of the sample stored in D_2O vapor and CO_2 for 12 hours, where D atoms are placed at the tetrahedral sites in the Na layer (Na_{tetra} in inset). (**L**) nPDF with contributions from major atomic pairs. Bonds marked with stars were calculated by placing the D atoms at the tetrahedral sites in the Na layer in NFM111.

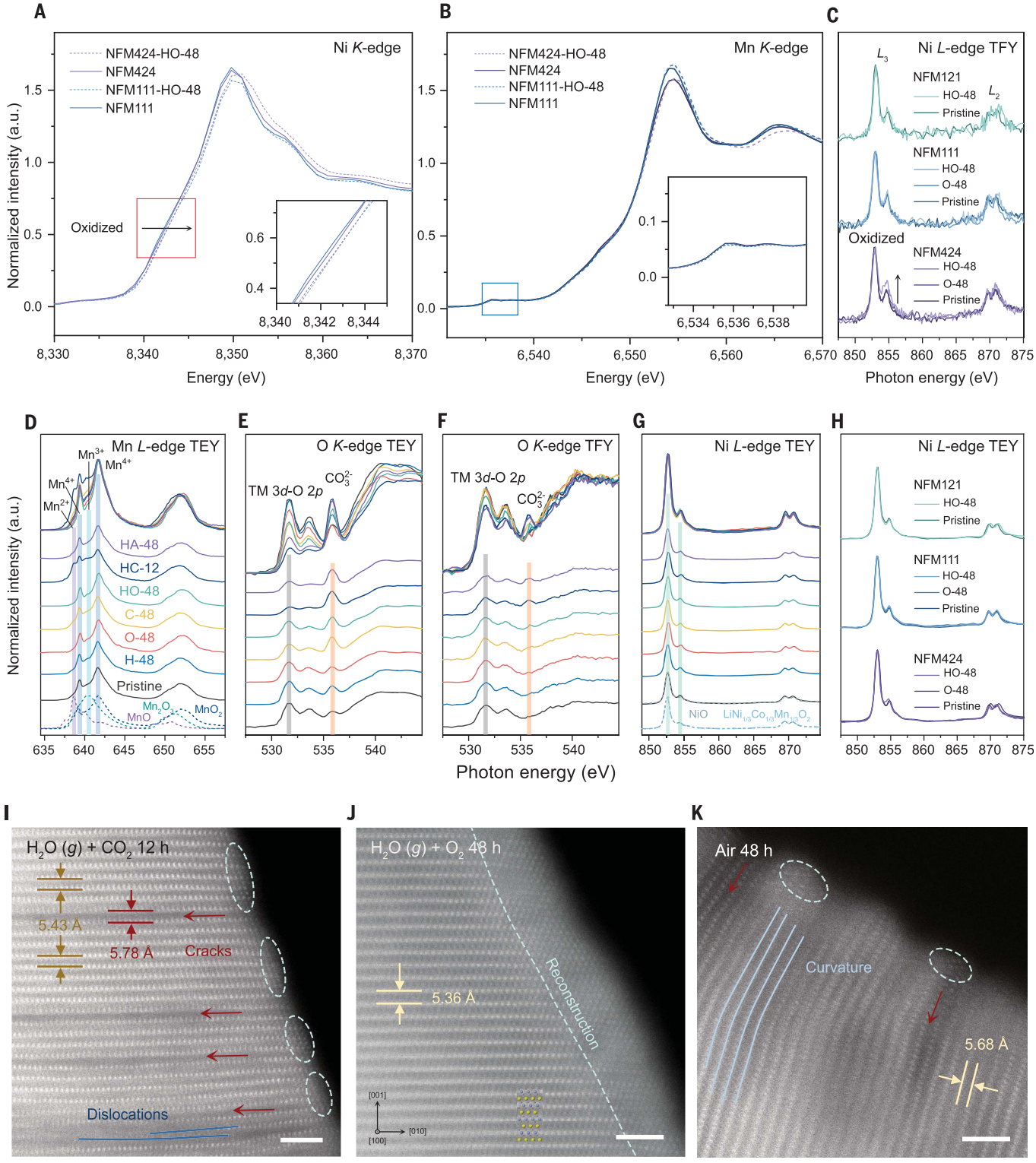

Fig. 3. Structural and chemical heterogeneity in oxidative and acid degradations. (**A** and **B**) Ni *K*-edge and Mn *K*-edge XANES spectra of NFM111 and NFM424 before and after being stored in O_2 with water vapor (RH = 80%) for 48 hours. (**C**) Soft XAS spectra of Ni *L*-edge in TFY mode of NFM424, NFM111, and NFM121 before and after storing in O_2 with water vapor (RH = 80%) for 48 hours. Spectra of NFM424 and NFM111 stored in O_2 (RH = 0%) for 48 hours were also compared. (**D** to **G**) Soft XAS spectra of Mn *L*-edge in TEY mode (D), O *K*-edge in TEY mode (E), O *K*-edge in TFY mode (F), and Ni *L*-edge in TEY mode (G) of NFM111 stored in different atmospheres: H-48 in N_2 with water vapor (RH = 90%) for 48 hours; C-48 in CO_2 (RH = 2%) for 48 hours; HO-48 in O_2 with water vapor (RH = 80%) for 48 hours; HC-12 in CO_2 with water vapor (RH = 60%) for 12 hours; and HA-48 in moist air (RH = 60%, CO_2 concentration ≈600 ppm) for 48 hours. (**H**) Soft XAS spectra of Ni *L*-edge in the TEY mode of NFM424, NFM111, and NFM121 before and after being stored in O_2 with water vapor (RH = 80%) for 48 hours. Spectra of NFM424 and NFM111 stored in O_2 (RH = 0%) for 48 hours were also compared. (**I** to **K**) STEM images of NFM111 after being stored in CO_2 with water vapor for 12 hours (I), O_2 with water vapor for 48 hours (J), and moist air (RH = 60%, CO_2 concentration ≈600 ppm) for 48 hours (K). Scale bars, 2 nm in (I) to (K).

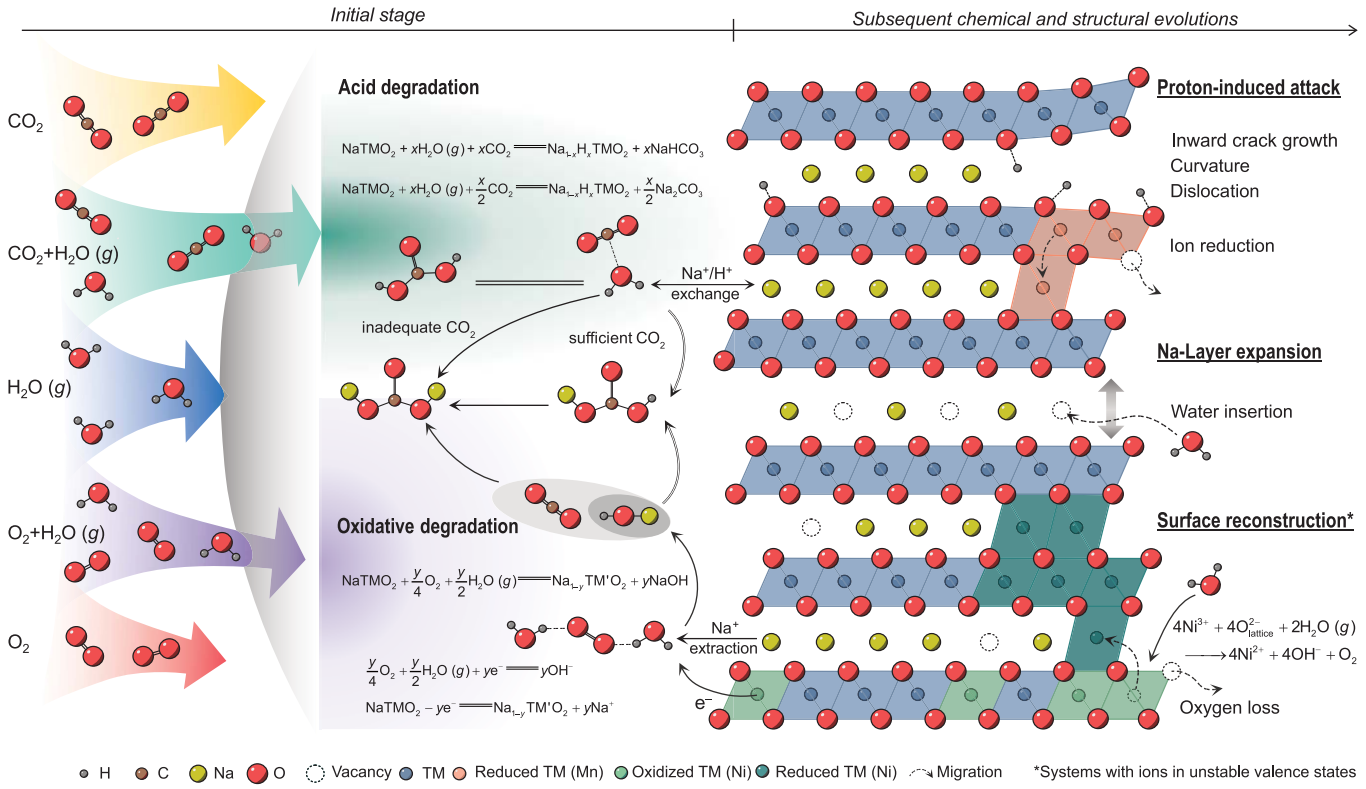

Fig. 4. Illustration of degradation mechanisms for O3-NLOs in the air. Left, contributions to the deterioration from various combinations of CO_2, O_2, and water vapor. Middle, surface reactions and corresponding products through acid and oxidative degradation pathways at the initial stage. Right, subsequent chemical and structural evolutions.

SEM images (Fig. 1, D to K, and figs. S5 and S6) also track the same trends in terms of morphology, where H-48, H-1W, and O-48 all exhibit identically clean and smooth surfaces. C-48 and CO-48 show a few protuberances, which is mainly due to the unavoidable residual moisture in CO_2 gas (RH = 2%); HO-48 is partly covered by residues along with amorphous clusters; and HC-48 is significantly enveloped by massive needle-like $NaHCO_3$. The combination of CO_2 and water vapor is therefore shown to be the most detrimental atmosphere in terms of deterioration, followed by the combination of O_2 and water vapor. Fourier transform infrared spectroscopy (FTIR) results also confirmed the presence of $Na_2CO_3{\cdot}H_2O$, $NaHCO_3$, and possibly NaOH in corresponding atmospheres, consistent with the findings from XRD and SEM characterizations (fig. S7).

The XRD and SEM results have generally identified the catastrophic impact of coupled water vapor and CO_2, but whether water vapor or CO_2 will solely commence microreactions initially at the surface needs to be clarified. In situ environmental TEM (ETEM) was performed to detect dynamic evolutions by avoiding ambient impact. NFM111 was first exposed to a CO_2 flow at a gas pressure (p) of 7 mbar for 30 min. Figure 2, A and B, and fig. S8 show that both surface and bulk structures are preserved, indicating that CO_2 cannot solely extract Na^+ from NFM111. Under a continuous flow of water vapor at 0.5 mbar for >2 hours (the corresponding mass spectrum is shown in fig. S9A), NFM111 retains its pristine state (Fig. 2, C and D). More targeted spots (fig. S10 and S11) show the same result, confirming that water vapor alone is not destructive to NFM111. By contrast, when exposed to the flow of CO_2 with water vapor under a total p of 0.5 mbar (the corresponding mass spectrum is shown in fig. S9B), the deterioration is fast and prominent. Figure 2, E to G, shows that the surface of NFM111 becomes rough within 1 hour of exposure to CO_2 with water vapor and is covered by a mass of $NaHCO_3$ (thicker than 15 nm) after 2 hours. The increased spacing of the lattice fringes from 5.33 to 5.40 Å reflects the expansion of the (003) plane along the c axis (Fig. 2, H and I). Severe surface degradations, including crack expanding, roughening, and secondary phase growth, are also tracked in other regions (fig. S12), corroborating the damaging effect of combined water vapor and CO_2.

To determine whether the degradation in water vapor with CO_2 is caused by the ion exchange of Na^+ with protons (H^+) or hydronium ions (H_3O^+) or by the intercalation of H_2O, CO_2, or CO_3^{2-} molecules, isotope-labeling strategies were adopted to track the relevant light elements. Time-of-flight secondary ion mass spectroscopy (ToF-SIMS) analyses were first conducted to determine whether external O (from H_2O or H_3O^+) and C (from CO_2 or CO_3^{2-}) enter the bulk after exposing NFM111 to $H_2{}^{18}O$ vapor and CO_2 with $H_2{}^{18}O$ vapor, respectively. The three-dimensional (3D) rendering of depth profiles (Fig. 2J) shows that only a very small amount of $Na_2{}^{18}O^+$ was detected on the surface in $H_2{}^{18}O$ vapor–treated sample, indicating a minimal interaction. Further, the $Na_2{}^{18}O^+$ and CH^- fragments of the sample stored in CO_2 with $H_2{}^{18}O$ vapor are mainly surface distributed, covering the bulk NiO_2^- (more fragments are shown in fig. S13). Both results exclude the intercalation of CO_2, CO_3^{2-}, H_3O^+, or H_2O. Neutron powder diffraction (NPD) was conducted to track the potential intercalation of H^+ after storing fresh NFM111 powders in D_2O vapor (D-72) and in CO_2 with D_2O vapor (DC-6 and DC-12). Even after being exposed to D_2O vapor for 72 hours, NFM111 still exhibits spectra identical to those of the fresh sample (fig. S14, A to D, and tables S3 and S4), whereas new peaks of $NaDCO_3$ appear in the range of 2.5 to 3.5 Å after only 6 hours of storage in CO_2 with D_2O vapor, and they intensify after storage for 12 hours (Fig. 2K and fig. S14B). Residual density in difference Fourier maps can be found at the tetrahedral sites in

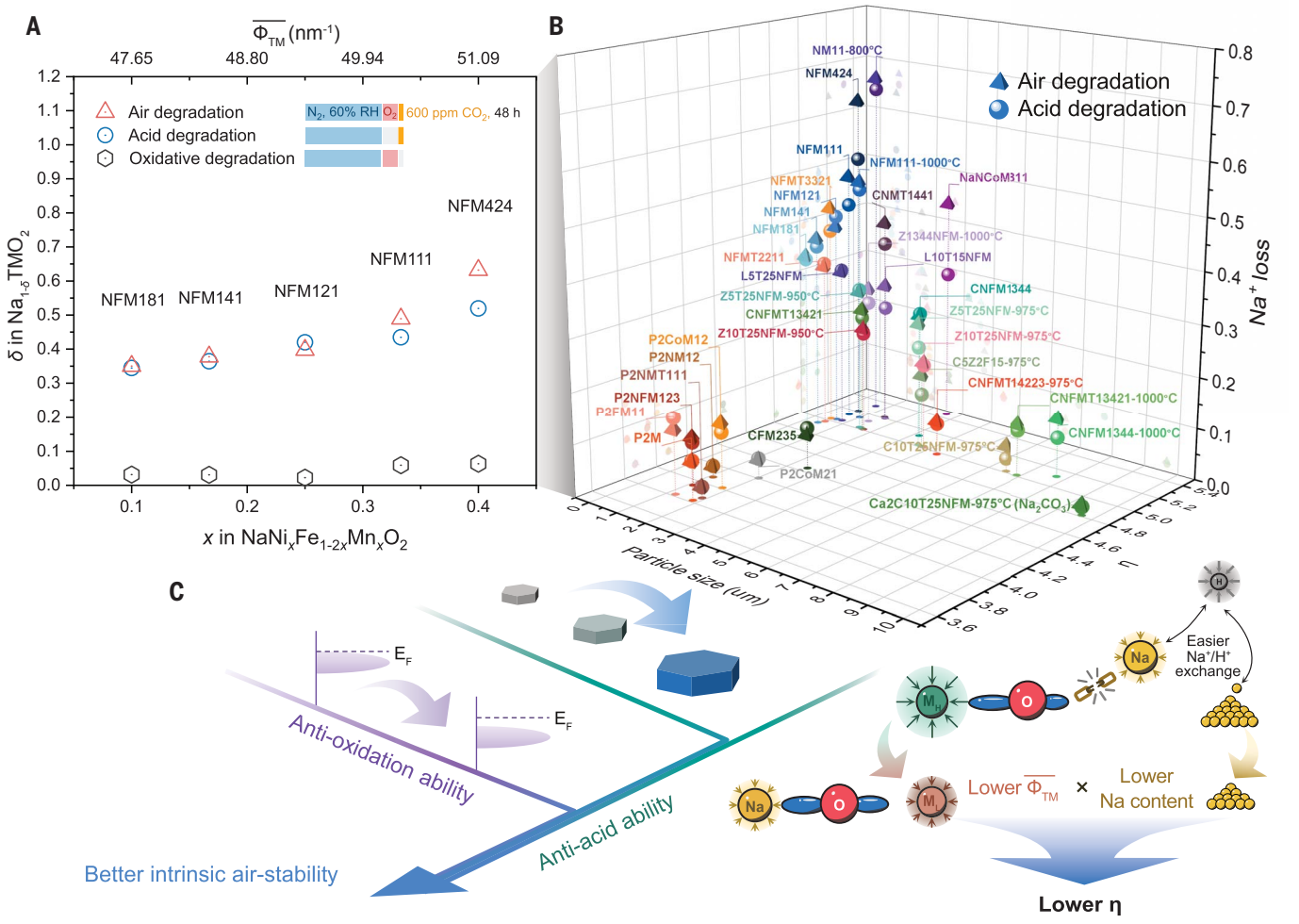

Fig. 5. Quantification of the effects of acid and oxidative degradation and countermeasures for developing air-stable NLOs. (**A**) Na^+ loss of $NaNi_xFe_{1-2x}Mn_xO_2$ materials (x = 2/5, 1/3, 1/5, 1/6, and 1/10) being tested by the proposed SQMAS with standard H660-48 tests (the RH and CO_2 concentration were maintained at 60% and 600 ppm, respectively) by taking their weighted average ionic potential ($\overline{\Phi_{TM}}$) as variables. (**B**) Na^+ loss of various NLOs being tested by HA660-48 and HC660-48 tests by taking cation competition coefficient (η) and particle size as two independent variables. (**C**) Summary of general strategies to elevate the intrinsic air stability for NLOs, where coating and other surface modifications are not included.

the Na layer (Na_{tetra}) of DC-6 and DC-12 after the dual-phase refinement taking Na-deficient NFM111 and $NaDCO_3$ as models (fig. S14, E, F, I, and J). Because the C from CO_2 and the O from H_2O have been excluded from occupying these sites and the slight migration of TM ions occurs only at the surface (Fig. 3, I to K), the intercalated protons are believed to occupy this site (fig. S14, G, H, K, and L, and tables S5 to S8). The Na_{tetra} may be an average site for protons in layers that still preserve pristine O stacking. Given the strong amorphization after the gas treatment and the mobility of protons surrounded by electronegative O in the O–Na–O layer at room temperature (*28*), a real O–D (H) bond length of r = 0.94 Å, as marked in neutron pair distribution function (nPDF) result (Fig. 2L), is more plausible. We thus conclude that sufficient protons, mostly generated from the combined water vapor and CO_2, exchange with Na^+ and intercalate into the Na layer to initiate acid degradation. The XRD results of other exposed $NaNi_xFe_{1-2x}Mn_xO_2$ materials (x = 2/5, 1/5, 1/6, and 1/10, denoted as NFM424, NFM121, NFM141, and NFM181, respectively) confirm this conclusion, showing varying degrees of acid degradation (fig. S15).

Apart from the acid degradation, previous XRD and SEM results showed that the coupling of O_2 and water vapor, rather than O_2 alone, can also degrade NFM111, implying an oxidation process. X-ray absorption spectroscopy (XAS) characterizations were conducted to investigate which TM ions can be oxidized. The valence states of Ni, Fe, and Mn are predominantly +2, +3, and +4 in fresh NFM111, respectively, as confirmed by x-ray absorption near edge structure (XANES) and soft XAS spectra (Fig. 3, A to H, and fig. S16). The Ni K-edge of NFMN111-HO-48 shows a slight shift to the higher-energy region in the XANES spectra (Fig. 3A), suggesting that the bulk Ni^{2+} can be oxidized after exposure to O_2 with water vapor. By contrast, Mn^{4+} and Fe^{3+} are largely unchanged in the bulk, as indicated by the unshifted Mn K-edge (Fig. 3B) in XANES spectra of NFM111-HO-48 and trivalence-featured Fe L-edge spectra (fig. S16, A and B). Moreover, the oxidation is more pronounced as the Ni content increases in $NaNi_xFe_{1-2x}Mn_xO_2$, because NFM424-HO-48 shows a more obvious shift in Ni K-edge spectra (Fig. 3A) and an intensified right shoulder of Ni L_3-edge in total fluorescence yield (TFY) mode, with a maximum detection depth of ~100 nm (Fig. 3C). Conversely, NFM121 shows negligible oxidation features (Fig. 3C). The calculated density of states of representative NFM424, NFM111, and NFM121 at ground state (fig. S17, A to D) reveals that the Ni $3d$ e_g orbitals contribute more to the valence band below the Fermi energy (E_F) level and rise significantly around E_F as the Ni content increases, indicating that the

increasing Ni content renders the material more susceptible to oxidation in $NaNi_xFe_{1-2x}Mn_xO_2$, and once the oxidative degradation commences, Ni^{2+} tends to be oxidized first. The initial charge profiles and XRD results comparing $NaNi_xFe_{1-2x}Mn_xO_2$ reaffirm the lower electrochemical redox potential and consequently more severe oxidative degradation induced by increasing Ni content (fig. S17E).

In addition to ion exchange and direct oxidation during acid and oxidative degradations, chemical and structural heterogeneity at the surface is also observed. In acid degradation, Mn^{4+} is reduced substantially for HC-12 and slightly for C-48 and HA-48 (in a sample that was exposed to the air for 48 hours, RH = 60% and CO_2 concentration = 600 ppm), as indicated by the pronounced peaks of Mn^{2+} at 639.6 eV and Mn^{3+} at 641.1 eV in Mn *L*-edge spectra in total electron yield (TEY) mode, with a maximum detection depth of ~5 nm (Fig. 3D). The decreased O *K*-edge pre-edge in TEY mode (Fig. 3E) also reflects a weakened TM 3*d* and O 2*p* orbital hybridization caused by TM reduction and oxygen loss (*29*). By contrast, the Mn *K*-edge spectra are less changed (Fig. 3B), and the TM 3*d* and O 2*p* orbital hybridization is recovered in bulk regions (Fig. 3F). As for the oxidative degradation, although the Ni^{2+} can be oxidized in the bulk, it remains +2 at the surface, evidenced by the almost overlapping Ni *L*-edge spectra in TEY mode of exposed and pristine NFM111, NFM424, and NFM121 (Fig. 3, G and H). This phenomenon can be ascribed to the instability of Ni^{3+}, as reported in $LiNiO_2$ (*6*), leading to the formation of surface rock salt NiO. More directly, high-angle annular dark-field scanning TEM images further confirmed the heterogenetic structures. Images of HC-12 (Fig. 3I and fig. S18, A to C) show a slight reconstruction occurs at the surface, and interlayer cracks and dislocations unevenly penetrate the bulk region, indicating that locally concentrated H^+ can lead to an inward growth of cracks and even ultimate exfoliation as the gases continuously reach the tips. STEM images of NFM111 (Fig. 3J and fig. S18, D to F) and NFM424 (fig. S19) that were exposed to water vapor and O_2 for 48 hours consistently showed a rock salt–like phase at their surfaces, indicating the reduction of Ni^{3+} and the formation of NiO. Combined features from both acid degradation and oxidation can be seen in NFM111 being exposed to the air for 48 hours (Fig. 3K and fig. S18, G to I). Negligible change can be found in STEM images of NFM111 even being stored in water vapor (90% RH) for 48 hours (fig. S20).

The pivotal role of water vapor

On the basis of the above observations, CO_2 or O_2 is only destructive to O3-$NaTMO_2$ in the presence of water vapor. In other words, water vapor is the bridge that connects CO_2 or O_2 with O3-$NaTMO_2$ and thus leads to two different degradation pathways. It is noteworthy that water vapor indeed reacts with surface Ni^{3+} and induces a subsequent reduction during oxidative degradation. This phenomenon is also found in other O3 systems such as O3-$NaNi_{0.5}Mn_{0.5}O_2$ (NM11) and $NaNi_{0.8}Co_{0.1}Mn_{0.1}O_2$ (NaNCM811). However, this interaction does not necessarily destroy the bulk structure and is still subordinate to the dominant two degradations, aligning with our findings (figs. S21 to S23). Additionally, despite being regarded as an unstable P2-NLO, $Na_{2/3}MnO_2$ (P2-NMO) exhibits a relatively lower reactivity toward water vapor (fig. S24). Therefore, we conclude that water vapor can be considered "conditionally inert" in the context of most NLOs if there are no inherently unstable ions present within the structure.

The corresponding structural and chemical evolution are comprehensively summarized in Eqs. 1 to 7 and Fig. 4. In the primary pathway through the "bridge," namely acid degradation, the presence of CO_2 alters the equilibrium of Na^+/H^+ exchange. As the density function theory calculation suggests, the reaction energy of exchanging Na^+ with H^+ from water (Eq. 1, x = 1/36 in this case) is 16.33 meV unit^{-1}, indicating a near-equilibrium reaction. The role of CO_2 can thus be seen as a destroyer of the equilibrium reaction between water vapor and $NaTMO_2$, which moves Eq. 1 forward and produces $NaHCO_3$ (when CO_2 is sufficient) or Na_2CO_3 (when CO_2 is inadequate) by increasing the acidity (Eqs. 2 and 3). In addition to the Na^+/H^+ exchange, locally concentrated protons may cause uneven extraction of Na^+ and surface reduction of Mn^{4+} or Mn^{3+}, resulting in severe cracking, curvature within interlayers, and surface reconstruction, as depicted in Fig. 4.

$$NaNi_{1/3}Fe_{1/3}Mn_{1/3}O_2 + xH_2O(g) \rightleftharpoons Na_{1-x}H_xNi_{1/3}Fe_{1/3}Mn_{1/3}O_2 + xNaOH \quad (1)$$

$$NaTMO_2 + xH_2O(g) + xCO_2 \longrightarrow Na_{1-x}H_xTMO_2 + xNaHCO_3 \ (\text{sufficient } CO_2) \quad (2)$$

$$NaTMO_2 + xH_2O(g) + \frac{x}{2}CO_2 \longrightarrow Na_{1-x}H_xTMO_2 + \frac{x}{2}Na_2CO_3 \ (\text{inadequate } CO_2) \quad (3)$$

In the secondary pathway through the "bridge," electrochemical oxidation occurs. The coexisting H_2O and O_2 can produce OH^- by oxidizing certain TM ions in $NaTMO_2$. The overall reaction (Eq. 4) is the combination of two half-reactions given in Eqs. 5 and 6. Contrary to the acid degradation, this oxidation reaction occurs simultaneously on the surface and in the bulk. However, unstable oxidized ions (typically Ni^{3+}) can be subsequently reduced in ambient water vapor (Eq. 7), accompanied by the reconstruction at the surface region, resulting in the formation of a rock salt phase (*6*, *18*).

$$NaTMO_2 + \frac{y}{4}O_2 + \frac{y}{2}H_2O(g) \longrightarrow Na_{1-y}TM'O_2 + yNaOH \quad (4)$$

$$\frac{y}{4}O_2 + \frac{y}{2}H_2O(g) + ye^- \longrightarrow yOH^- \quad (5)$$

$$NaTMO_2 - ye^- \longrightarrow Na_{1-y}TM'O_2 + yNa^+ \quad (6)$$

$$4Ni^{3+} + 4O^{2-}_{\text{lattice}} + 2H_2O(g) \longrightarrow 4Ni^{2+} + 4OH^- + O_2 \quad (7)$$

The generated NaOH can absorb a large quantity of water, resulting in a fluid quasiliquid that gathers in the gaps between particles and can further react with CO_2. This explains the amorphous products on the HO-48 sample in SEM images (fig. S6, E to H) and the gathering of the $Na_2{}^{18}O^+$ fragments shown in fig. S13C.

Rationalizing the design principles

To intelligently build future air-stable NLOs, the next stage is to determine which internal features of different materials respond to the two degradation pathways and how. This requires objective quantification and comparison of the degree of deterioration among NLOs. However, such a quantitative comparison remains challenging and has been rarely achieved (*30*). Inspired by the success of titration gas chromatography in quantitatively distinguishing the grown phase with minimal environmental influence (*31*, *32*), we proposed a method based on this, which we call the standard quantification method for air-stability (SQMAS). SQMAS involves a series of standard atmospheric treatments to control the degradation process and convert various possible Na surface residues to Na_2CO_3, which is then titrated with acid to produce CO_2 and measured by gas chromatography to determine the amount of Na^+ loss after deterioration. The details are illustrated in fig. S25 and S26 and described in the supplementary text. We chose 48 hours as the testing time because it is sufficient for the degradation to reach the equilibrium (fig. S27).

SQMAS was first performed in $NaNi_xFe_{1-2x}Mn_xO_2$ to quantify the contributions of acid and oxidative pathways to the total Na^+ loss and highlight the severity of overall air degradation, showing that >0.30 bulk Na^+ can be lost after air exposure for 48 hours (HA660-48 test, where RH = 60%, CO_2 concentration ≈600 ppm) in all samples (Fig. 5A and table S9). As the Ni content of $NaNi_xFe_{1-2x}Mn_xO_2$ increases, this value can reach as high as 0.633 in NFM424. Oxidative degradation accounts for <10% of the overall Na^+ loss and becomes almost negligible as the Ni and Mn content in $NaNi_xFe_{1-2x}Mn_xO_2$

decreases to 0.25, consistent with the conclusion that an elevated electrochemical redox potential induced by a lower Ni content weakens the oxidative degradation. Conversely, acid degradation dominates the overall deterioration, accounting for 84 to 100% of the total Na^+ loss in the air. These results also highlight that even a minor quantity of CO_2 (0.06% in volume) can activate water vapor, leading to catastrophic acid degradation. Apparently, elevating the air stability of NLO heavily relies on improving the anti-acid stability.

If the lattice oxygen binds Na^+ more tightly, then the process of dissociating O–Na bonds and reestablishing O–H bonds during acid degradation can be effectively hindered. In this case, the strength of interactions between TM and lattice oxygen becomes the key to modulating the O–Na bond in the TM–O–Na sandwich configuration (*33*). Inspired by the successful use of ionic potential (Φ) to compare the polarization between TMO_2 and NaO_2 slabs (*34*), such a thermodynamic interaction can be described by the weighted average ionic potential of TMs, $\overline{\Phi_{TM}} = \sum \omega_i n_i / R_i$, where ω_i is the content of TM_i with charge number n_i and radius R_i. A lower $\overline{\Phi_{TM}}$ indicates a weakened TM–O attraction and thus a strong Na–O interaction, leading to less possibility of a Na^+/H^+ exchange. For instance, as $\overline{\Phi_{TM}}$ decreases in NFM424, NFM111, and NFM121, the Na–O bond becomes tighter, as reflected by the increased Bader charges on lattice oxygen (table S10), resulting in improved anti-acid stability in the rank of NFM424 < NFM111 < NFM121. $\overline{\Phi_{TM}}$ can effectively capture the trend when x = 1 in Na_xTMO_2, but the impacts of Na content should also be considered, because NLOs can exhibit different Na contents. Given that a substantial Na reserve can enhance both the possibility and frequency of Na^+/H^+ exchange, the decrease in Na content offers the materials with fewer Na resources for exchange. Additionally, the polarizing influence of alkaline ions was also taken into account, especially in light of distinguishing characteristics between NLOs and their Li counterpart. We thus propose the "cation competition coefficient" (η) to depict the competition between cations of TM ions and alkaline ions and serve as a predictive tool in elucidating the trends of Na^+ loss in various NLOs. η is defined as follows:

$$\eta = \frac{x_A \overline{\Phi_{TM}}}{\phi_A} \quad (8)$$

where x_A is the content of alkaline ions in A_xTMO_2 and ϕ_A is the ionic potential of alkaline ions.

By extending SQMAS to various NLOs (tables S11 and S12 and figs. S28 to S33), we found that η and particle size are two major factors that influence the anti-acid stability and thus the air stability of NLOs. As shown in Fig. 5B (and detailed in fig. S34 and table S13), P2-NLOs and Na-deficient O3-NLOs exhibit a lower η than most O3-NLOs and thus show less Na^+ loss. For O3-NLOs with similar particle sizes, the replacement of Mn^{4+} and Ni^{2+} with ions having lower ionic potential, such as Ti^{4+}, Fe^{3+}, Zn^{2+}, Cu^{2+}, and Li^+, effectively mitigates Na^+ loss. This is evident when comparing $NaNi_xFe_{1-2x}Mn_xO_2$ (with decreasing x values), NFMT3321, NFMT2211, and L5T25NFM. When exhibiting a close η value, NLOs with larger particle sizes show an improved anti-acid ability, which is attributed to the prolonged diffusion paths for Na^+ (H^+), retarding the Na^+/H^+ exchange rate. A clear illustration of this effect is seen in the comparison among NFM111, ZNFM1344-1000°C, CNFM1344, and CNFM1344-1000°C. These findings also imply that elements such as Cu^{2+} and Zn^{2+}, along with high-temperature calcination, favor the formation of single crystals, whereas Ti^{4+} tends to form fine grains, as observed in NFMT3321 and NFMT2211.

On the basis of the above analyses, the rational design of intrinsic air-stable NLOs is clear (Fig. 5C). The antioxidation stability can be obtained by introducing TMs with higher redox potentials ($Cu^{2+}$and Fe^{3+}) or by decreasing the content of TMs with lower redox potentials (Ni^{2+} and Mn^{3+}). Conversely, the anti-acid stability can be enhanced through both stoichiometric and structural design: decreasing η to reduce the likelihood of Na^+/H^+ exchange, increasing the particle size by introducing the appropriate ions (Cu^{2+} and Zn^{2+}), and elevating calcination temperature to decrease the Na^+/H^+ exchange rate. Combining these strategies, several designed samples, such as CNFM1344-1000°C, CNFMT13421-1000°C, CNFMT14223-975°C, and C10T25NFM-975°C, which have suitable Ni content and substantial capacity, only experience 0.05 to 0.10 Na^+ loss and show improved cycling performance, demonstrating promising applicability (figs. S35 and S36).

Discussion

We have decoupled the acid and oxidative degradations of NLOs upon exposure to air and showed the individual and collective roles of different air components in degradation. In material storage, the key is to break the collective effect of coupled air components. Strict environmental humidity control remains the most effective method, but it brings extra cost and may fail in long-distance shipping. Although it is challenging to completely eliminate the water vapor, simply using low-cost soda lime, which absorbs CO_2 during packing, can provide comparable protection regardless of the RH (fig. S37). More potential strategies for alleviating the air degradation of NLOs and their challenges in commercial production are summarized in fig. S38. The most effective strategy in surmounting these hurdles continues to center on enhancing the intrinsic air stability of NLOs. To determine the factors ruling intrinsic air stability, we quantified and compared the Na^+ loss value across diverse NLOs. Although the Na^+ loss is relatively low in P2-NLOs, the larger Na-layer distance facilitates the water molecule insertion (fig. S39). More complex aspects should be considered in comparing the air stability of P2-NLOs and O3-NLOs, as detailed in the supplementary text. The intrinsic air stability can be realized by a combination of strategies using low-cation competition coefficients and large particle sizes, and it is anticipated to be further enhanced when protective coatings, surface engineering, and modification in the NLOs are implemented. Extra concerns should be addressed in systems containing a high content of unstable ions such as Mn^{3+}, and Ni^{3+}, in which inherent instability, including susceptibility to reduction and Jahn-Teller distortion, may induce more severe effects. In addition to understanding the fundamental mechanisms and establishing guidelines for developing air-stable NLOs, our findings can also assist us in understanding the difference in air stability for NLOs and their Li counterparts (fig. S40). The relatively low redox potential of NLOs renders them susceptible to oxidative degradation. The weaker Na–O interaction, implied by the lower ionic potential of Na^+ than Li^+, facilitates a much faster Na^+/H^+ exchange than Li^+/H^+. Although air exposure can also lead to the formation of alkaline carbonate and hydroxide on the surface of Ni-rich LLOs, the low solubility of these compounds allows them to function as a shield to impede further degradation. Conversely, whereas the Na_2CO_3 formed at the surface may initially encapsulate the cathode particles, its strong water absorptivity and solubility can re-expose the surface of NLOs, resulting in continuous degradation in the humid air (*13*). Therefore, the design of intrinsically air-stable NLOs becomes imperative. The successful synthesis of $Na_{0.96}Ca_{0.02}Cu_{0.1}Ni_{0.35}Fe_{0.1}Mn_{0.2}Ti_{0.25}O_2$ with a mere 0.019 Na^+ loss underscores the efficacy of the combined strategies, where low η, increased particle size, a potential segregation effect, and the pillar effect of Ca^{2+} (*35*) are used synergistically.

Our findings offer a comprehensive roadmap for the design of air-stable NLOs, with a focus on practicality in advancing the next-generation NIBs. These insights serve as a catalyst for additional explorations aimed at overcoming similar stability challenges in related materials, thereby propelling the field forward.

REFERENCES AND NOTES

1. S. W. Kim, D. H. Seo, X. Ma, G. Ceder, K. Kang, *Adv. Energy Mater.* **2**, 710–721 (2012).
2. N. Yabuuchi, K. Kubota, M. Dahbi, S. Komaba, *Chem. Rev.* **114**, 11636–11682 (2014).
3. N. Ortiz-Vitoriano, N. E. Drewett, E. Gonzalo, T. Rojo, *Energy Environ. Sci.* **10**, 1051–1074 (2017).

4. Y. Bi *et al*., *Science* **370**, 1313–1317 (2020).
5. X. Liang, J.-Y. Hwang, Y.-K. Sun, *Adv. Energy Mater.* **13**, 2301975 (2023).
6. H. S. Liu, Z. R. Zhang, Z. L. Gong, Y. Yang, *Electrochem. Solid-State Lett.* **7**, A190 (2004).
7. L. Zou *et al*., *Nat. Commun.* **11**, 3204 (2020).
8. W. Zhang *et al*., *Adv. Energy Mater.* **13**, 2202993 (2023).
9. K. Kubota, S. Komaba, *J. Electrochem. Soc.* **162**, A2538–A2550 (2015).
10. Y. Takeda, J. Akagi, A. Edagawa, M. Inagaki, S. Naka, *Mater. Res. Bull.* **15**, 1167–1172 (1980).
11. J. M. Paulsen, J. R. Dahn, *Solid State Ion.* **126**, 3–24 (1999).
12. Z. Lu, J. R. Dahn, *Chem. Mater.* **13**, 1252–1257 (2001).
13. L. Mu *et al*., *Adv. Mater.* **27**, 6928–6933 (2015).
14. R. Usiskin *et al*., *Nat. Rev. Mater.* **6**, 1020–1035 (2021).
15. Y.-S. Hu, Y. Li, *ACS Energy Lett.* **6**, 4115–4117 (2021).
16. F. Duffner *et al*., *Nat. Energy* **6**, 123–134 (2021).
17. Z. Fang *et al*., *J. Am. Chem. Soc.* **143**, 10261–10274 (2021).
18. Y. You, A. Dolocan, W. Li, A. Manthiram, *Nano Lett.* **19**, 182–188 (2019).
19. V. Duffort, E. Talaie, R. Black, L. F. Nazar, *Chem. Mater.* **27**, 2515–2524 (2015).
20. M. Sathiya, K. Hemalatha, K. Ramesha, J. M. Tarascon, A. S. Prakash, *Chem. Mater.* **24**, 1846–1853 (2012).
21. M. H. Han *et al*., *J. Mater. Chem. A* **4**, 18963–18975 (2016).
22. W. Zuo *et al*., *Nat. Commun.* **11**, 3544 (2020).
23. D. Kim *et al*., *Electrochem. Commun.* **18**, 66–69 (2012).
24. H. Wang *et al*., *J. Electrochem. Soc.* **163**, A565–A570 (2016).
25. Y. Sun *et al*., *ACS Appl. Energy Mater.* **4**, 2061–2067 (2021).
26. C. Xu *et al*., *ACS Appl. Mater. Interfaces* **14**, 5338–5345 (2022).
27. W. Zuo *et al*., *Nat. Commun.* **12**, 4903 (2021).
28. K.-D. Kreuer, *Chem. Mater.* **8**, 610–641 (1996).
29. L. Mu *et al*., *Adv. Energy Mater.* **8**, 1801975 (2018).
30. W. M. Seong, Y. Kim, A. Manthiram, *Chem. Mater.* **32**, 9479–9489 (2020).
31. C. Fang *et al*., *Nature* **572**, 511–515 (2019).
32. X. Zhang *et al*., *Cell Rep. Phys. Sci.* **2**, 100668 (2021).
33. H.-R. Yao *et al*., *Energy Storage Mater.* **54**, 661–667 (2023).
34. C. Zhao *et al*., *Science* **370**, 708–711 (2020).
35. L. Zhang *et al*., *J. Electrochem. Soc.* **170**, 070514 (2023).

ACKNOWLEDGMENTS

We thank the Beijing Synchrotron Radiation Facility (BSRF) for use of the 4B9A beamline, the Shanghai Synchrotron Radiation Facility (SSRF) for use of the BL14W1 and BL02B02 beamlines, and the China Spallation Neutron Source for use of the the multiphysics instrument (MPI). **Funding:** This work was supported by the National Key R&D Program of China (2022YFB2402500); the Strategic Priority Research Program of the Chinese Academy of Sciences (XDA0400000); the National Natural Science Foundation (NSFC) of China (52394174, 52122214, 92372116, U20A20336, and 21935009); the Youth Innovation Promotion Association of the Chinese Academy ofSciences (2020006); the Young Elite Scientists Sponsorship Program by CAST (2022QNRC001); and the Natural Science Foundation of Hebei Province (B2024203054). **Author contributions:** Y.-S.H. and J.H. conceived the idea and directed this research. Y.Y., Xiaowei Li, and B.W. synthesized the samples. Y.Y. performed the atmospheric treatment and conducted XRD, SEM, and electrochemical measurements and data analyses. Z.W., C.D., and Y.Y. performed the in situ ETEM experiments and data analyses. Xinyan Li and Q.Z. performed the STEM experiments. S.W. and R.X. performed the density function theory calculation and analyses. Y.Y. and Xuefeng Wang designed the SQMAS measurement. Y.Y., X.Z., B.W., and Xubin Wang tested the samples by SQMAS. Y.Y., N.Z., Y.N., and F.D. conducted the XAS measurements and data analysis. J.X., W.Y., Y.Y., X.R., and Y.N. conducted the NPD and nPDF measurements and data analysis. Y.Y., Y.L., X.R., J.Z., and Y.-S.H. wrote the manuscript. All authors discussed the results and commented on the manuscript. **Competing interests:** The authors declare no competing interests. **Data and materials availability:** All data are available in the main text or the supplementary materials.

SUPPLEMENTARY MATERIALS

Submitted 13 November 2023; accepted 11 July 2024
10.1126/science.adm9223